

SUPPLEMENTARY INFORMATION

doi:10.1038/nature12952

This section is in three parts. The first part presents Angular Resolved Photoemission Spectroscopy and STM experiments on arrays of epitaxial graphene sidewall ribbons and a comparison of ARPES data with other exfoliated graphene. The second part describes details of the transport analysis presented in the main text, which is brought into context with other graphene ribbon work. We also present details of three samples (B through D) showing that the effects presented in the paper are general. We also provide additional measurements on Sample A, presented in Fig. 4, main text.

The second part describes the preparation and in situ growth and characterization of the graphene nanoribbons in Fig. 3 (main text). It also provides all the data for 50 resistance measurements on various ribbons at 3 different lengths.

A. Surface characterization: ARPES and STM

B. Transport analysis

1. Comparison with exfoliated and other graphene ribbons.
2. Graphene Ribbon Sample A
3. Graphene ribbon Sample B
4. Graphene ribbon Sample C
5. Graphene ribbon Sample D
6. Length dependence
7. Comparison with carbon nanotubes
8. Explanation of the resistance doubling and tripling effect
9. FAQs

C. Preparation and characterization of epitaxially-grown graphene nanoribbons by local in-situ transport measurements

1. Growth of GNRs for in-situ resistance measurements and their -situ characterization
2. Characterization by 4-tip STM SEM
3. Additional 4-probe in-situ resistance measurement of GNR

A. Surface characterization: ARPES and STM

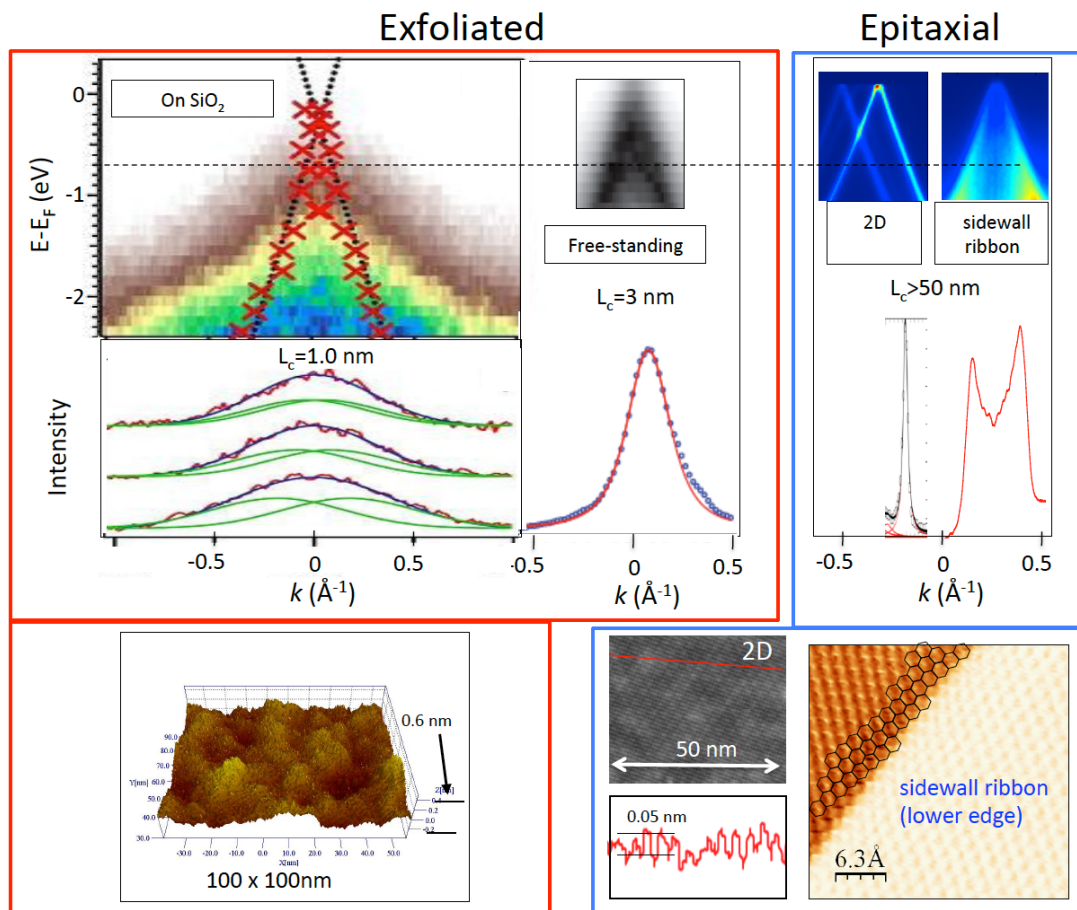


Figure S1. Comparison of epitaxial graphene (blue frame) and exfoliated graphene (red frame) from a surface science perspective. STM topographical images of exfoliated graphene on SiO_2 ¹ (Bottom left); and epitaxial graphene² (bottom middle) and a sidewall ribbon (bottom right from Fig. 2). The deposited exfoliated material is topologically rough with 0.6 nm fluctuations obscuring the structure of the carbon layer. The epitaxial graphene (both on the 2D, C-face and the sidewall ribbon) clearly shows the honeycomb structure and no substrate induced roughness. The 2D material, in addition shows a faint moiré pattern, which is not seen in the sidewall ribbon. *Top:* Angle resolved photoelectron spectra (ARPES); the horizontal and vertical scales are the same for all spectra. Top left: Exfoliated graphene on SiO_2 ³ shows a broad unresolved peak, $\delta k \approx 0.5 \text{ \AA}^{-1}$, that corresponds to a correlation length $L_c = 2\pi/\delta k = 1 \text{ nm}$. (The x's result from a fit to the graphene band structure.); (Center left): ARPES of suspended graphene⁴ ($\delta k \approx 0.5 \text{ \AA}^{-1}$) corresponding to a correlation length of 3 nm (after accounting for broadening due to corrugations). (Center right): ARPES of 2 dimensional epitaxial graphene on the C-face, the peak width corresponds to the instrument resolution ($\delta k \approx 0.01 \text{ \AA}^{-1}$), corresponding to $L_c > 50 \text{ nm}$. (Left): ARPES of an array of a thousand of 24 nm wide sidewall ribbons; peak widths correspond to the instrument resolution corresponding to $L_c > 50 \text{ nm}$ parallel to the ribbon axis. Note that disorder in exfoliated graphene severely distorts the band structure near close to the Dirac point whereas epitaxial graphene has a well defined Dirac point.

B. Transport analysis

1. Comparison with exfoliated and other graphene ribbons

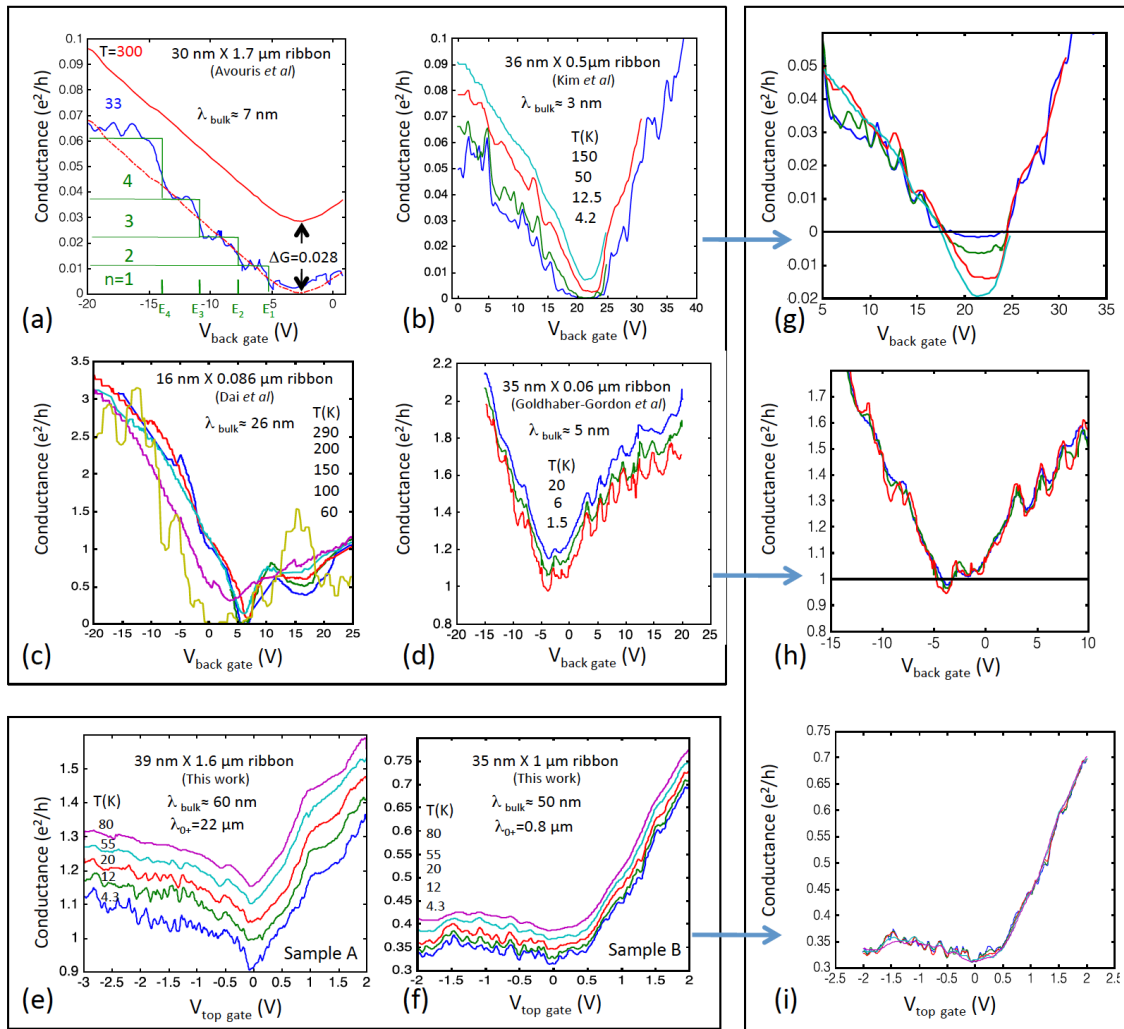


Figure S2. Comparison of the conductances of 6 gated ribbon samples measured at several temperatures from the literature, demonstrating temperature independence of the $n \neq 0$ subbands and temperature dependence of the $n=0$ subband. (a) 30 nm X 1.7 μm patterned exfoliated graphene ribbon⁵; (b) 36 nm X 0.5 μm patterned exfoliated graphene ribbon⁶; (c) 16 nm X 0.086 μm unzipped nanotube⁷; (d) 35 nm X 0.060 μm gate defined exfoliated graphene constriction⁸; (e) 39 nm X 1.6 μm epitaxial sidewall graphene ribbon (Sample A); (f) 35 nm X 1.6 μm epitaxial sidewall graphene ribbon (Sample B); (g) Data from (b) after $G_0(T)$ subtraction; (h) Data from (d) after $G_0(T)$ subtraction; (i) Data from (f) after $G_0(T)$ subtraction. Also note that the mean free paths measured in transport agree well with the correlation lengths that are measured in ARPES (Fig. S1). The relatively poor transport properties of exfoliated graphene ribbons are due to the strong interactions with the disordered substrate and disorder at the interface with the graphene layer. These cause the mobility gap at $n=0$ in exfoliated graphene ribbons. In contrast, epitaxial graphene sidewall ribbons are ordered and do not have a mobility gap.

Figure S2 shows 6 graphene ribbon samples including 4 samples produced by patterning exfoliated graphene deposited on oxidized silicon wafers (Fig. S2a-d). The data were extracted from published work, representing transport properties as a function of temperature and back gate voltages. Samples A and B (Fig. S2e-f) were produced and measured by us. The main point here is the observation that the temperature dependence of the conductivity for $V_g \neq 0$ ($E_F \neq 0$) is represented by a conductivity shift that depends on T only (and not on V_g). In the Landauer picture, this shift is consistent with the contribution of the $n=0$ subbands (i.e. the transmission $Tr_0 \rightarrow 0$ for $T \rightarrow 0$) while the transmission coefficients of the $n \neq 0$ subbands, $Tr_{n \neq 0}$, are insensitive to temperature.

- In Fig. S2a a shift of 0.028 G_0 causes the $T=100$ K data to overlap with the $T=33$ K data.
- In Fig. S2b shifts are applied to produce Fig. S2g.
- Figure S2c is for an opened carbon nanotube ribbon⁷ where the $n \neq 0$ subbands are reasonably parallel to each other.
- Fig. S2d shows a very short ribbon (a gate-produced constriction⁸). This ribbon is not defined by lithographic patterning of the graphene itself, so that graphene is not damaged and the effective ribbon edges are smooth. Excellent overlap of the data is found by applying uniform $G(T)$ shifts (see Fig. S2h) resulting in a trend that is consistent with Eq. 2, of the main text. The residual conductance is very close to 1 G_0 and is clearly related to our observations.

An analysis of the scattering lengths shows the following. The back-gate induced charge density is assumed to be equivalent to that of an infinite sheet, yielding an upper limit for the effective scattering lengths along the ribbon. These scattering lengths λ_{bulk} are estimated from the measured subband conductivity $\Delta G = G(E_F) - G(E_F=0)$ in units of G_0 , where, for bulk back gated graphene, $E_F(\text{meV}) \approx 31.2 V_g^{1/2} (\text{V})^{1/2}$, so that $\lambda_{bulk} \approx 10.5 \Delta G V_g^{1/2} L/W$ where L is the length and W is the width of the ribbon. The scattering lengths determined by this procedure are noted in the figures.

In Fig. S2a, the staircase structure in the 33 K data are due to the opening of successive subbands (as explained by the authors⁵), consistent with the Landauer picture (see main text). The subband indices are shown. Since the step heights $\Delta G_n/G_0$ ($= 0.011, 0.011, 0.016, 0.022$ for $n=1-4$) correspond to $4Tr_n$, so for small λ_n , $\lambda_n \approx Tr_n L = 4.7, 4.7, 6.8, 9.3$ nm for $n=1-4$, which agrees with the value determined from the slope dG/dV_g . Moreover, the measured energy spacing $E_{n+1} - E_n = 44, 42, 33$ meV, agreeing with the energy spacing for a 30 nm zigzag ribbon predicted to be $E_{n+1} - E_n = 47$ meV (for small n).

For comparison, Fig. S2e is a reproduction of Fig. 4c of the main text for Sample A for which $\lambda_{bulk} \approx 60$ nm and $\lambda_{o+} = 22$ μm . Fig. S2f shows a second epitaxial graphene sidewall ribbon, Sample B, (35 nm \times 1.06 μm) for which $\lambda_{bulk} \approx 50$ nm and $\lambda_{o+} = 0.8$ μm . As shown in Fig. S2i, the $G(V_g)$ all collapse together by applying a V_g -independent conductance shift for each temperature. Note that our data shows

reproducible fine structure from one temperature to the next, testifying to their high quality.

2. Graphene Ribbon Sample A

This sample was presented in Fig. 4 (main text). Here magnetic data are included. In addition in Fig. S3 we also show magneto-resistance data $G(B)$. These data are also presented after converting G to $T_{el}(G)$, analogous to the bias voltage data (Fig. 4g). The magnetic field axis is converted to an equivalent temperature, $T_B = \mu_B B / k_B$. Hence plotted, the dimensionless slopes correspond to an effective magnetic moment μ (in units of μ_B). This analysis presumes that the increasing conductance is caused by a magnetically induced increase in the chemical potential (and not due to weak localization). Note the essentially perfectly linear, V-shaped, about 4 Tesla wide, magneto-conductance dip. The dip corresponds to $T_{el} = T + \mu|B|$ where $\mu = 5\mu_B$ at low temperatures and increases to $\mu \approx 10 \mu_B$ at high temperatures. For all ribbon samples at all temperatures the constant slope abruptly changes at $|B| \approx 2$ T (Figs. S3-S6).

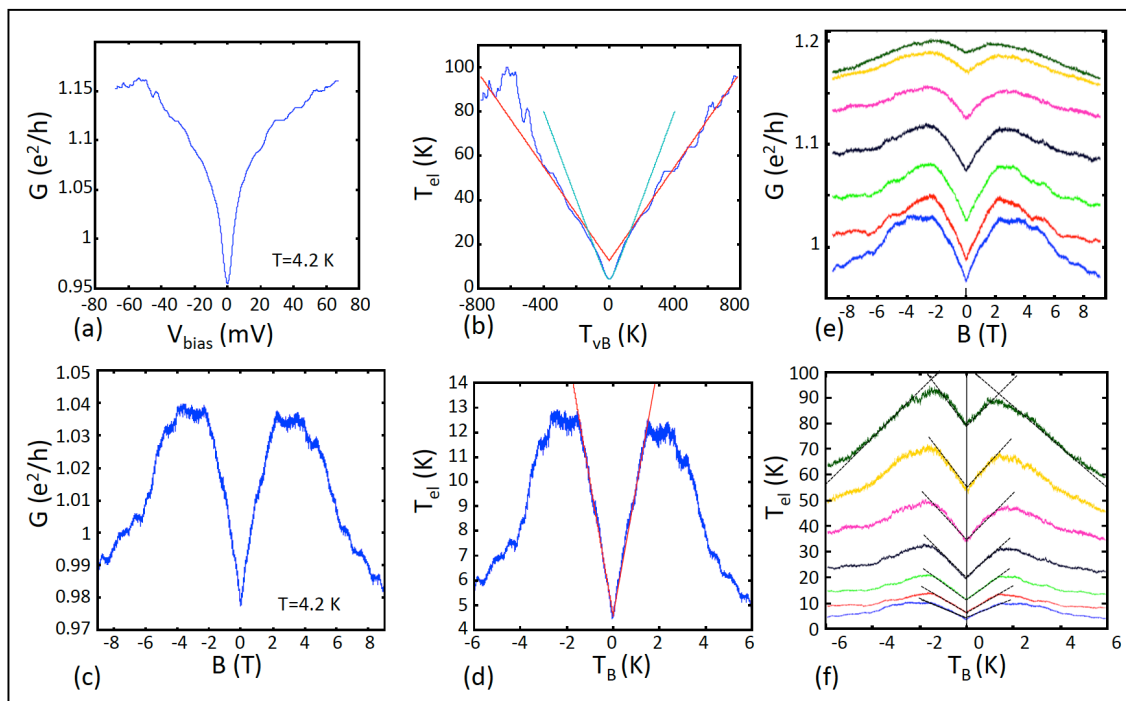


Figure S3. Sample A is a 39 nm X 1.6 μ m gated sidewall ribbon connected to wide graphene leads. The $T=4.2$ K conductance versus bias voltage (a) and versus magnetic field (c) show linearity at low bias voltage (magnetic field, resp); (b) and (d) are the same data as (a) and (c), resp, but plotted in units of electronic temperature T_{el} derived from $G(T)$ and as a function $T_{VB} = eV_b/k_B(K)$ and $T_B = \mu_B B / k_B$, resp. (e) Conductance versus magnetic field for T (in K) = 4.2, 7, 12, 20, 35, 55 and 80 (bottom to top). (f) Same data as (e) after converting G to T_{el} and B to T_B as in (d).

An extension to the detailed analysis already presented in the main text concerning sample A, highlighting the $T=4.2$ K data is presented here. The conductance G of this sample is given by $G(T) = \alpha G_0 (1 + 0.5 \exp{-\theta^{1/2}})$, where $\alpha = 0.922$; $\theta = T^*/(T-T_0)$ with measured $T_m^* = 21.5$ K, (compared with $T_p^* = 20.9$ K from $T_p^* = 1.4\pi\hbar c^*/k_B L$ ($L = 1.6$ μm) and $T_0 = 2.2$ K. This equation is algebraically inverted to determine the electronic temperature T_{el} from the conductance: $T_{el}(G) = T^*(\ln(2G/\alpha G_0 - 2)^{-2} + T_0)$. Likewise, the bias voltage is converted to $T_{Vb} = eV_b/k_B$ and the magnetic field is converted to $T_B = \mu_B B/k_B$. In this way Figures S3b and S3d are generated (from S3a and S3c). The slopes in Fig. S2d correspond to the inverse electronic heat capacity ν in units of k_B (as defined in the main text). Slopes in Fig. S3c correspond to magnetic moments (in units of μ_B). Note the sharp V shaped dip in the magnetic data (with slopes corresponding to $5.6 \mu_B$), which is typical for all low temperature, low field graphene ribbons. The lines $T_{el} = T + \mu|B|$ versus $T_B = \mu_B B/k_B$ corresponds $\mu = 5.6 \mu_B$ and $T = 4.2$ K is the sample temperature. The downturn at $T_B = \pm 2$ K, is seen in most graphene ribbon, 2D graphene and nanotube data. The hyperbolic fit to Fig. S3b, corresponds to Eq. 3: $T_{el} = \sqrt{(T_{Vb}/\nu)^2 + T^2}$ with $\nu = 5$ and $T = 4.2$ K (i.e. the sample temperature) following Eq.3.

3. Graphene ribbon Sample B

Sample B is a graphene ribbon ($1.06 \mu\text{m} \times 35 \text{ nm}$) sample similar to sample A in design. The main features observed in sample A are also observed here. The temperature dependent conductivity corresponds to $\alpha = 0.311$ and $T_m^* = 29$ K, following Eq. 2. Note that the predicted T_p^* according to $T_p^* = 1.4\pi\hbar c^*/k_B L$ is 31.6 K, in excellent agreement with the measured value (despite the significantly reduced value of α).

The G versus V_g for several temperatures is similar to Sample A, Fig. 4c (main text). Note that all of the data collapse onto a common curve after subtraction of a gate voltage independent conductance (temperature dependent) as was seen in Sample A as well (Fig. 4c). The implications of this are discussed in the main text (see also discussion of Fig. S2).

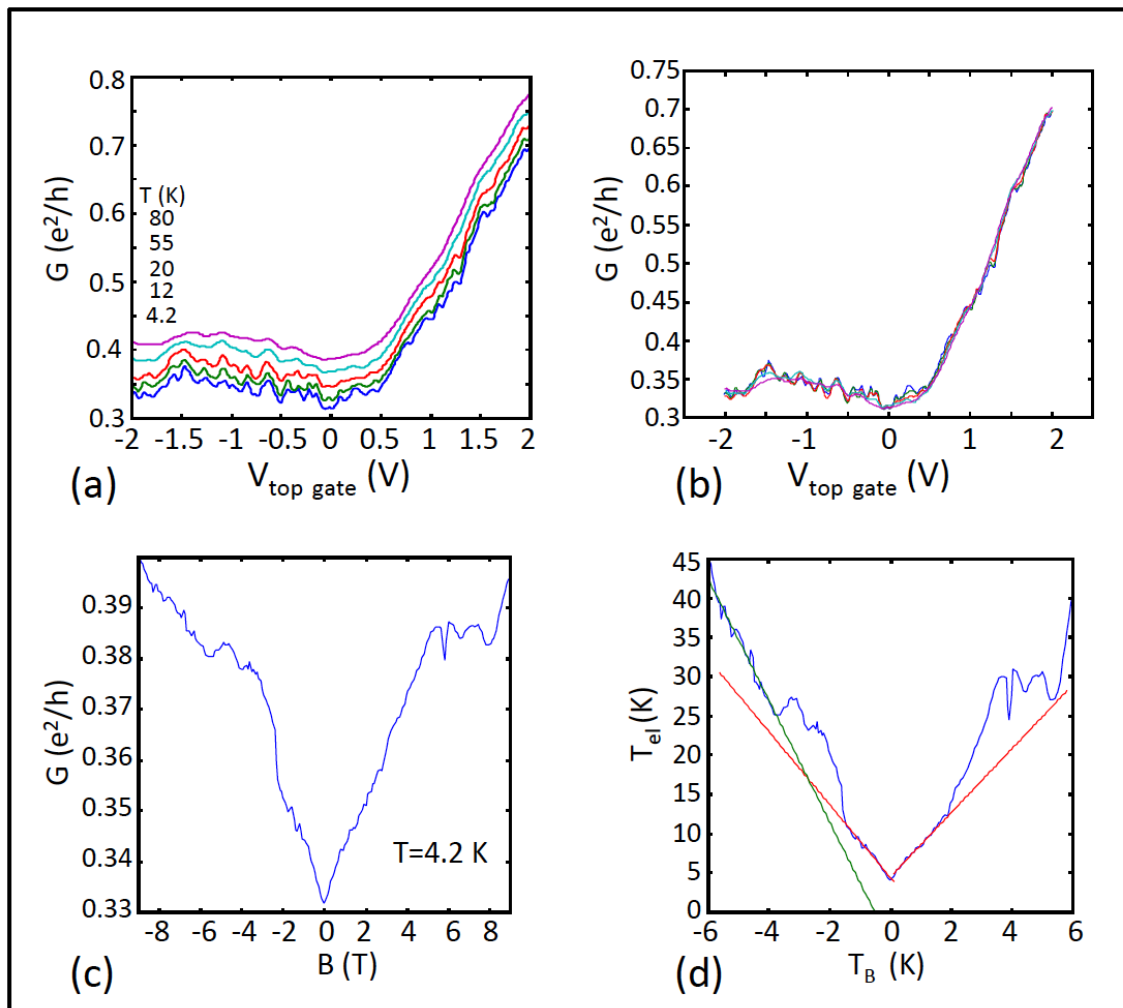


Figure S4 Properties of Sample B (35 nm X 1.06 μm sidewall ribbon supplied with a top gate). (a) G versus V_g , for various temperatures. (b) Collapse of the data in (a) by subtraction of a V_{bias} constant $G(T)$ for each temperatures T . (c) Conductance as a function of magnetic field for $T=4.2$ K. (c) $T_{\text{el}}=T+\mu|B|$ versus $T_B=\mu_BB/k_B$ slopes (as for sample A) correspond to $4.3 \mu_B$ (red) and $7.7 \mu_B$ (green).

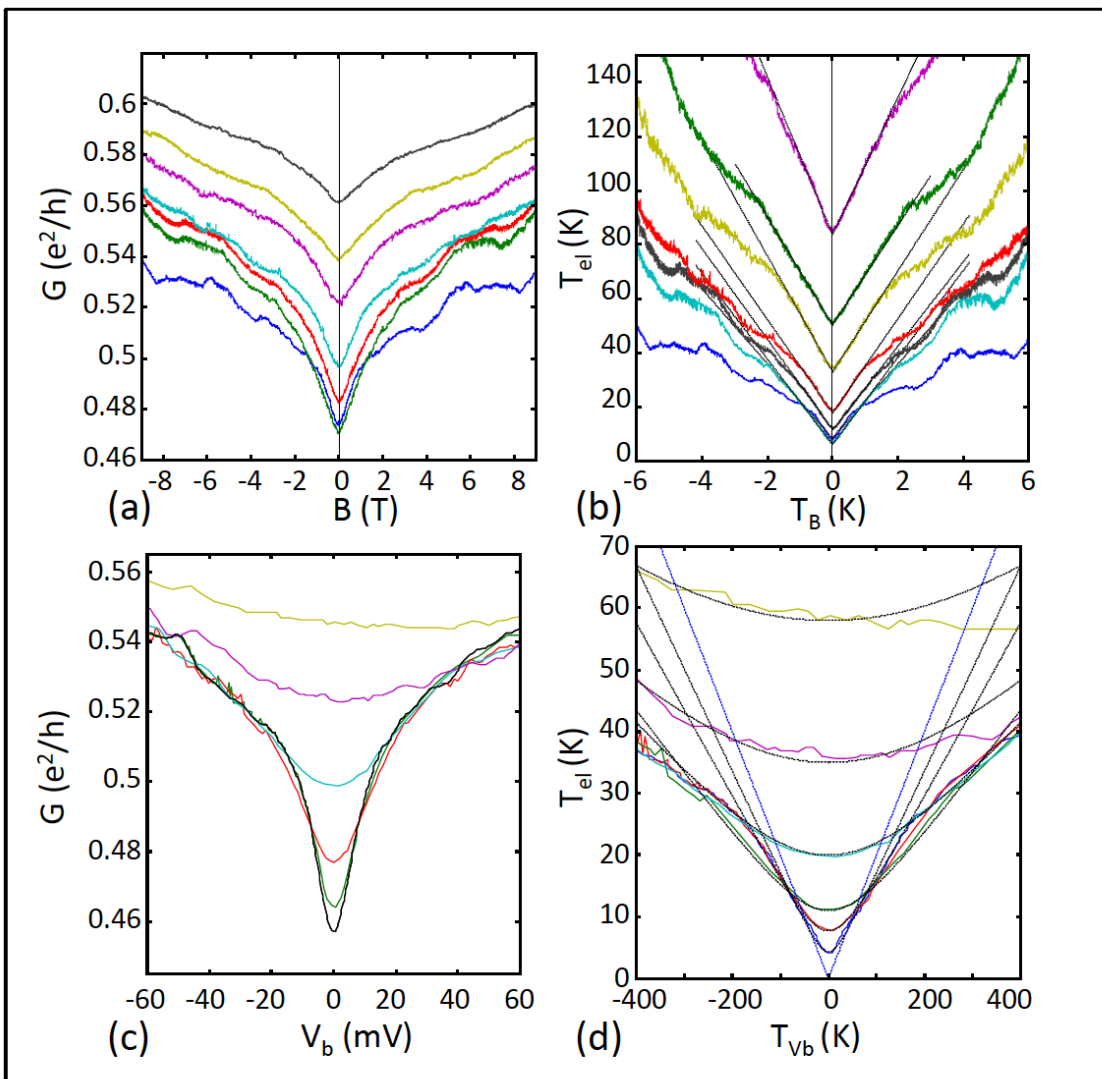


Figure S5. Graphene ribbon Sample C, $L = 1 \mu\text{m}$, $W = 39 \text{ nm}$; $T_m^* = 49 \text{ K}$, $\alpha = 0.454$. (a) Conductance versus magnetic field, measured at T (in K) = 4.2, 7, 12, 20, 35, 55 and 80 showing characteristic dip at $B=0$. (b) Data from (a) after conversion (as for sample A) to $T_{el} = T + \mu|B|$ versus $T_B = \mu_B B/k_B$, showing linear response. Magnetic moments correspond to μ (in μ_B) = 14, 16, 16, 17, 20, 20, 27. (c) Bias voltage response for T (in K) = 4.2, 7, 12, 20, 35 and 55. (d) Data from (c) after conversion to T_{el} and T_{Vb} . Hyperbolic response agrees with Eq. 3 with $\nu = 5, 6, 7, 9.5, 11, 12$.

4. Graphene ribbon Sample C

The magnetic field and bias voltage dependence of graphene ribbon Sample C (measured from 4.2 K to 180 K) shows the characteristic features of graphene ribbons (Fig. S5). After converting $G(B)$ to $T_{el} = T + \mu|B|$ and B to $T_B = \mu_B B / k_B$ (like in the previous examples), the highly curved magnetic field response shows the typical behavior seen in previous samples. However the magnetic moments obtained from the slopes range from $14 \mu_B$ to $27 \mu_B$; that are a factor of 2 greater than typically observed. The bias voltage dependence shows the hyperbolic response (Fig. S5d) as predicted in Eq. 3, with $\nu = 5$ at 4.2 K, typical for graphene ribbons. The (approximately factor of 2) slope change at $T_{el} \approx 15$ K is also typically seen, as reported in the main text.

5. Graphene Ribbon Sample D

Sample D is a sidewall ribbon 36 nm X 0.37 μm . From $G(T)$, $\alpha = 0.628$ and $T_m^* = 87$ K. The value of T_p^* determined from Eq. 2 is 93 K that agrees very well with the measured value. Conductance measurements were made on this graphene ribbon, as shown in Fig. S6a, using a conducting AFM tip at room temperature in ambient conditions. The left wide graphene pad was connected to ground. The contact resistance, measured by placing the tip on the left graphene pad was subtracted. The resulting conductance versus tip position is plotted in Fig. S6b, showing that the conductance decreases from about $2 G_0$ to about $0.9 G_0$ with increasing tip to pad distance L . The curve is identical to that in Fig. 3a where the exponential decrease is given by: $G = G_0 \exp(1-L/L^*)$ for $L > L^*$, where $L^* = 160$ nm as indicated by the theoretical curve (green line). While the correspondence is not nearly as good as in Fig. 3a, it is nevertheless consistent with the measurement.

The magnetic field and bias voltage dependence of this sample (simulated as for sample A) are typical for graphene ribbons, as in the examples above. Measurements were made for temperature ranging from 4.2 K to 180 K. The curved response of the raw data (Fig. S6c) converts to the typical V shape with a magnetic moment $5.4 \mu_B$ at $T = 4.2$ K. The bias voltage response is also typical. The bias voltage dip converts to hyperbola given by Eq. 3; with $\nu = 7$ for $T = 4.2$ K (see the figure caption of Fig. S6 for the other values).

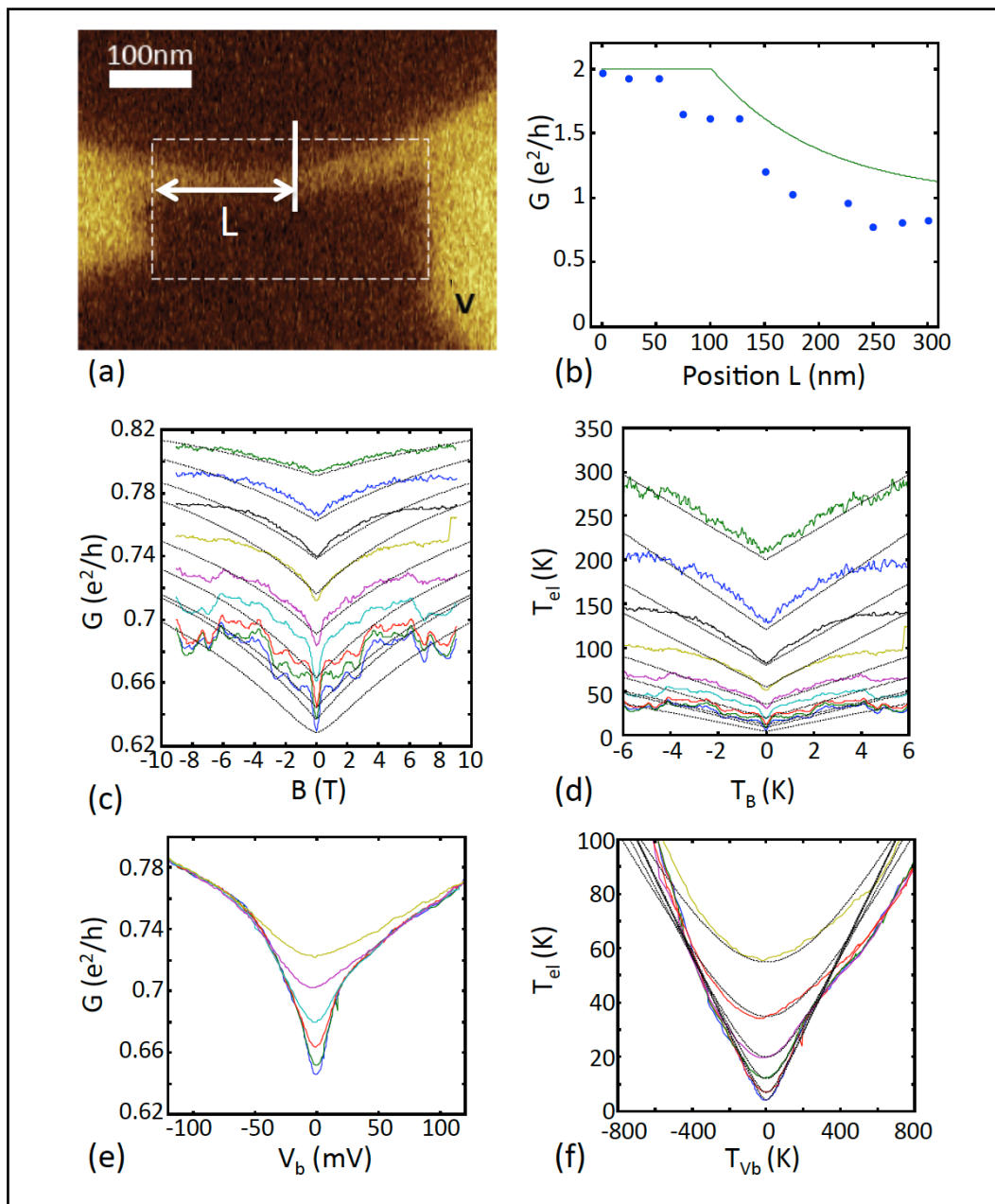


Figure S6. Transport properties of Sample D, a 36 nm X 0.37 μm sidewall ribbon. (a) Electrostatic force microscopy image. (b) Scanning probe conductance measurements using conducting AFM tip showing uniform conductance decrease from $G = 2G_0$ to $G = 0.8G_0$. Solid line corresponds to $G = G_0 \exp(1-L/L^*)$. (c) Magnetic field dependence for T (in K) = 4.2, 7, 12, 20, 35, 55, 80, 120 and 180. Temperature dependence gives $\alpha = 0.628$ and measured $T_m^* = 87$ K from Eq. 2 (which agrees very well with the predicted $T_p^* = 93$ K). Fits are obtained like in the procedure described for sample A above. The magnetic moments correspond to μ (in μ_B) = 5.4, 6.5, 6.4, 7.7, 9.2, 14, 15, 18 and 16 as typically found in graphene ribbons. (d) Same data as in (c) plotted in terms of $T_{el} = T + \mu|B|$ and $T_B = \mu_B B/k_B$ (e) Bias voltage dependence for T (in K) = 4.2, 7, 12, 20, 35 and 55. (f) Data in (e) plotted in terms of T_{el} and T_{vb} using Eq. 3, for $v=7.0, 7.0, 7.0, 7.5, 8.3$ and 8.1 , values that are typical for graphene ribbons.

6. Length dependence

The length dependence of the 0- subband for $T = 300$ K (for the samples presented in Fig. 3a, main text) is plotted on a logarithmic scale (Fig. S7), which brings out its exponential behavior more clearly for $L > L^* = hc^*/k_B T = 160$ nm. For both ribbons the conductance is approximately $G = G_0 \exp(1-L/L^*)$ for $L > L^*$ and $G = G_0$ for $L < L^*$ as explained in the main text.

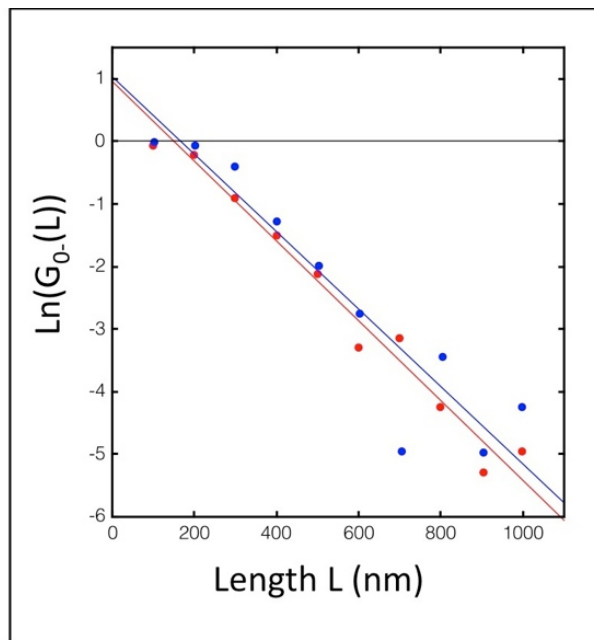


Figure S7. $\ln G_0$ versus length for the two short ribbon segments in Fig. 3a (main text) measured at room temperature.

7. Comparison with carbon nanotubes

As shown below the response of carbon nanotubes is remarkably similar to that of graphene ribbons. However the overall conductances are increased by a factor of 2. As was shown 15 years ago⁹ carbon nanotubes are ballistic conductors at room temperature and the conductance is (nominally) $2e^2/h$, in contrast to the theoretical prediction of $4e^2/h$. In that respect, similar to the factor of 2 discrepancy observed in graphene ribbons. From thorough transport measurements on (multiwall) carbon nanotubes, Schönenberger et al.¹⁰ concluded that (1) carbon nanotubes are quasi-ballistic with mean free paths on the order of 20 nm, (2) their magnetic response shows a conductance dip that can be modeled with a multi-parameter fit to standard weak localization theory, (3) their bias voltage response demonstrates Luttinger liquid behavior, (4) the temperature response is complex and shows evidence of localization and no evidence for room temperature micron scale ballistic conductance.

In light of our measurements on graphene ribbons we reexamined the data¹⁰ from which these conclusions were drawn and found carbon nanotubes behaved essentially identically to graphene ribbons as shown in Fig. S8 in all details. Specifically, the temperature dependence is consistent with Eq. 2 with $T_m^* = 49.9$ K (corresponding to $L = 670$ nm, from $T_p^* = 1.4\pi\hbar c^*/k_B L$, compared with the measured $L = 350$ nm) and $T_0 = 2.0$ K. However, the factor of 1/2 in Eq. 2 is replaced by a factor of 3. The conductance $G(T)$ saturates at $G = 2\alpha(2e^2/h)$ at $T \approx 50$ K (Fig. S8b), a factor 2 higher than the short ribbons in Fig. 3a.

Like for graphene ribbons, the bias voltage dependence is found to follow Eq. 3, with $\nu = 5$ (see Fig. S8c) for small bias voltages and about twice that for large bias voltages. The magnetic field dependence shows the sharp characteristic dip at $B = 0$ that corresponds to $T_{el} = T + \mu|B|$ with $\mu = 5 \mu_B$. The V shape is interrupted for $|B| \geq 2$ T showing complex behavior at higher field, as seen in all graphene ribbon samples. Consequently, the transport properties carbon nanotubes, as well as underlying mechanisms are certainly similar to graphene ribbons. Nanotubes are certainly two component ballistic conductors as well.

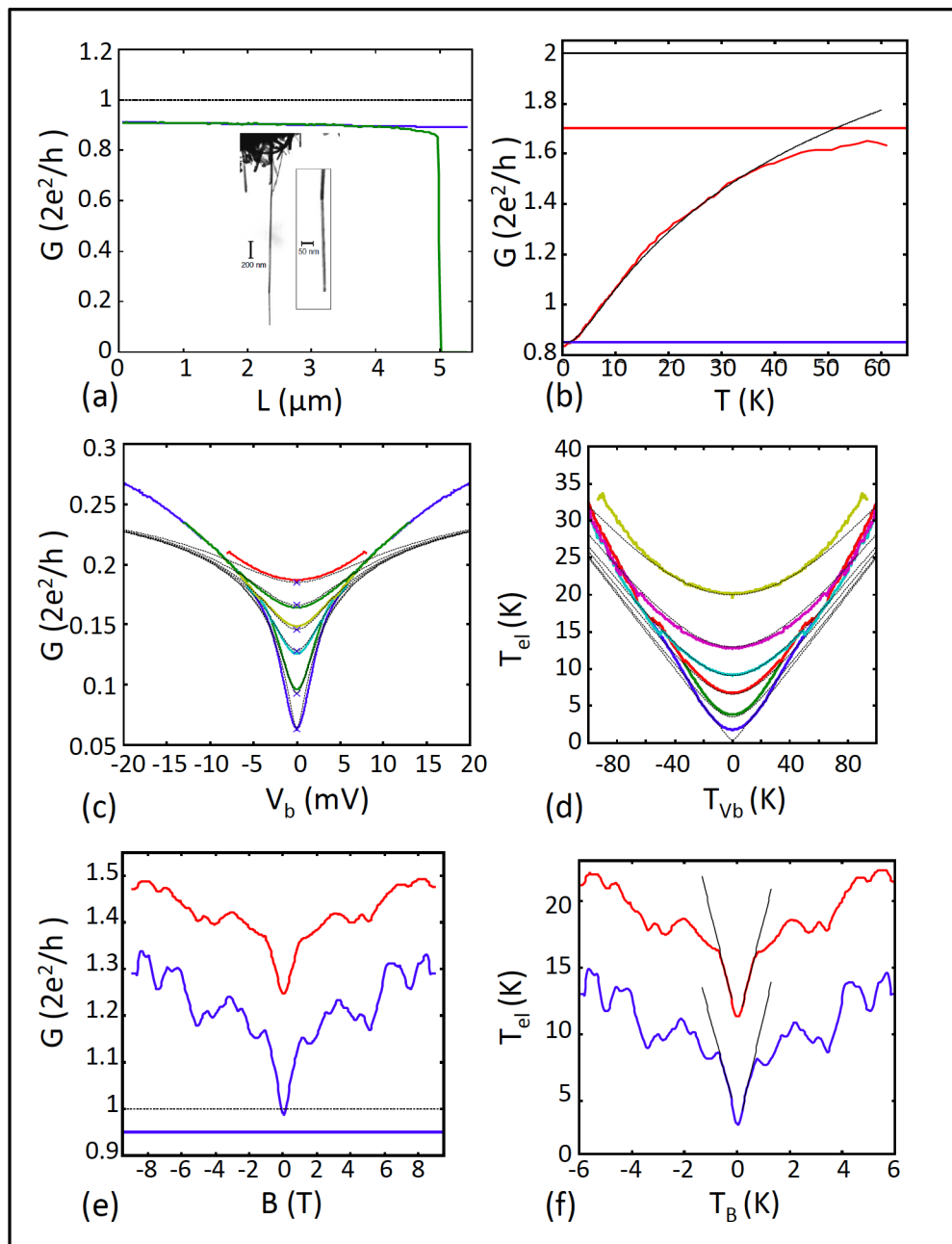


Figure S8 Reexamination of transport properties of multiwall carbon nanotubes (a) Room temperature transport as measured by Frank et al⁹ showing $2e^2/h$ ballistic transport indicating two channels. (b-f) Measurements by Schönenberger et al¹⁰. (b) Measured temperature dependence of the conductance, corresponding to $\alpha = 0.90$, $T_m^* = 49.9$ K. Note the saturation at 2α . (c) Measured bias voltage versus temperature with superimposed calculations following Eq. 2. The fits correspond to $\nu = 4$, very close to $\nu = 5$ observed in graphene ribbons. (d) Data of (c) converted to T_{el} and T_{Vb} showing hyperbolic behavior consistent with Eq. 3. (e) Magnetic field dependence for $T = 2.5$ K and $T = 12$ K, showing typical dip at $B = 0$; (f) Same data as in (e) plotted as a function of T_{el} and T_B , with superimposed simulation according to $T_{el} = T + \mu|B|$ and $T_B = \mu_B B / k_B$ with $\mu = 5 \mu_B$, as for graphene ribbons. As for ribbons, the behavior becomes complex for $|B| > 2T$.

8. Explanation of the resistance doubling and tripling effect

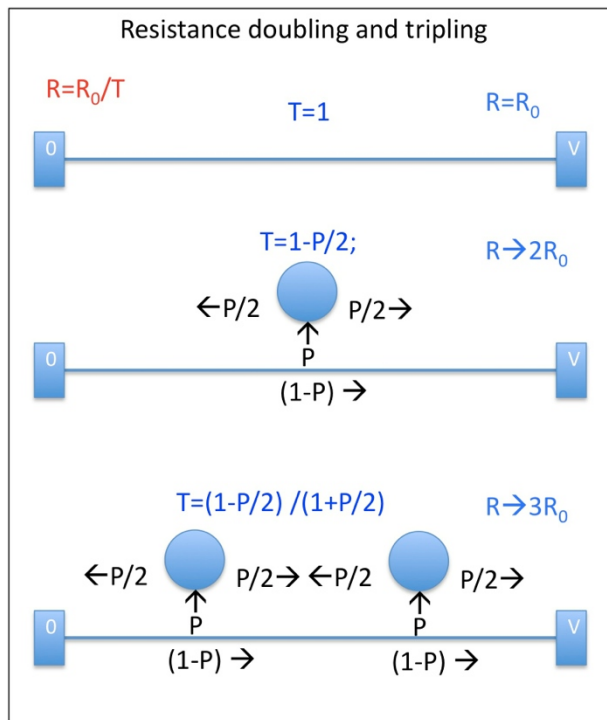


Figure S9. Ballistic wire connected to contacts (left and right) as in Fig. S11a. (Top) Undisturbed wire. (Middle) wire with one thermalizing probe. (Right) wire with two thermalizing probe.

Fig. S9 shows how invasive probes affect a current flow. For a ballistic one-dimensional non-degenerate wire, the conductance $G = G_0 \text{Tr}$, where Tr is the transmission. If the flow is undisturbed then $\text{Tr} = 1$ and $G = G_0 = e^2/h$. For a more complete discussion, see refs 11, 12.

However an invasive probe will alter the flow. P is the probability that a charge carrier moving past the probe will enter it. After thermalization in the probe, it exits it with equal probability going either to the right or to the left. As indicated in Fig. S9 the total forward probability is $(1-P)+P/2$ (the reflected probability is $P/2$). Hence, $\text{Tr} = 1-P/2$ and $G = (1-P/2)G_0$. If $P = 1$ (every electron enters and exits the probe) then $G = G_0/2$ (the resistance is doubled: $R = 2R_0$). In fact this is what should be expected, since a perfectly invasive probe simply divides the ballistic wire into two ballistic wires.

If two invasive probes are inserted (Fig. S9 bottom) then the situation is slightly more complicated, since the backward scattered charges from probe 2 (for example) will scatter from probe 1 etc. This results in a geometric series that is easily summed to give $\text{Tr} = (1-P/2)/(1+P/2)$; Hence, for $P = 1$, $\text{Tr} = 1/3$ and $R \rightarrow 3R_0$.

9. FAQs : Alternative explanations suggested by referees and others

The entire surface is graphitized with a diffusive conducting layer giving rise to high conductivities; the observed conductance quantization is simply fortuitous.

This proposed morphology is contradicted by numerous experiments, see for example Fig. 2, and extensive Raman and EFM characterization (see for instance refs 13-16).

Resistances between adjacent ribbons are more than $450\text{ k}\Omega$ (and more than $30\text{ M}\Omega$ for the low-temperature measurements), at least an order of magnitude greater than along a ribbon.

This cannot explain the dependence on the probe separation.

This cannot explain the resistance doubling and tripling effect.

The probability P that measured values fall within 20% of each other in more than 50 samples (assuming a random distribution with a dispersion of a factor of 2, which is very conservative) is $P = 10^{-50}$. Hence it is impossible.

The graphene is multilayered making the conductivities large

ARPES measurements show a monolayer (Fig. S1)¹⁷. Moreover, it would require at least 100 highly doped layers to attain the observed resistivities (dR/dL), which is physically impossible. Also, this cannot explain the consistent $1(h/e^2)$ contact resistance or the length dependence (or any of the other observed effects).

The ribbons are diffusive and the resistance doubling and tripling effect is caused by multiple side-by-side ribbons that are broken when they are touched by the probe and reunite when the probe is removed.

It is inconceivable that ribbons break and reform when touched by a probe. In order for several ribbons to consist of three ribbons in parallel to produce this effect would require an impossible combination of parallel diffusive ribbons.

The magnetic field dependence and temperature dependence is due to weak localization.

The fit to Eq. 2 is exceptionally good and requires a minimal number of parameters, each of which are well defined and consistent from one ribbon to the next. Neither the temperature dependence nor the magnetic field dependence nor the length dependence can be reproduced over the same range with using standard weak localization theory with accepted expressions for L_f and L_m (see for instance Ref. 10, 18. For example, for carbon nanotubes, two different power laws are need for L_f for $2\text{ K} \leq T \leq 10\text{ K}$ and $10\text{ K} < T < 50\text{ K}$ ¹⁰).

The bias voltage dependence is due to the well-known zero bias anomaly.

Attempts to fit the bias voltage dependence of conductivity with standard approaches (Luttinger liquid $G(V_b)$ power law dependence) failed to reproduce the observed bias voltage dependence over any reasonable range.

Properties measured on epitaxial graphene are not relevant because substrate interactions are large.

Properties within 1 meV from charge neutrality are reliably attributed to graphene as experimentally demonstrated (see main text). Substrate interactions and strain induced effects measured in ARPES, STM and in transport are very small (see Fig. S1) and much smaller than in deposited and suspended graphene as clear from the scientific literature (See also Figs. S1 and S2).

D. In-situ resistance measurements, growth and characterization

1. Growth of GNRs for the in-situ resistance measurements and their ex -situ characterization

The GNR structures for the in-situ resistance measurements were grown in Hannover selectively by sublimation epitaxy on MESA-structured 6H-SiC(0001) surfaces¹³. Before, 1 μm wide line structures were generated by optical lithography (UV-light, 286 nm) and reactive ion etching (RIE, SF₆ and O₂ ratio 20:7) onto the 6H-SiC(0001) surface (nitrogen doped, 10¹⁸ cm⁻³). The optical mask was aligned such that the trench structures run along the [1-100] direction, i.e. the zig-zag direction for graphene grown epitaxially on Si-terminated SiC(0001). The anisotropic etching and suitable etching rates of around 0.3 nm/sec allows us to fabricate defined terraces and trench MESA structures. By thermal annealing (DC-heating in an Ar atmosphere of 4x10⁻⁵ mbar, sample clamped by graphite contacts) of this structure clean and well-ordered crystal facets are forming around 1420 K^{13, 19}. Further annealing to 1570 K results in growth of extended graphene nanoribbons on these facets^{13, 20} as sketched in Fig. S10. The formation of well orientated graphene nanoribbon structures has been proven recently by LEED and ARPES measurements¹⁷.

In this study ribbons down to 40 nm in width were obtained by using MESA trench structures of 20 nm in depth. Electrical measurements on these nanostructures were performed with a 4-tip STM/SEM system (Fa. Omicron nanoprobe). Details are reported below. Before transfer of these structures into the 4-tip STM SEM system for further processing and electrical characterization the overall quality of the

ribbons has been checked by AFM and EFM (see Fig. S10d,e). The line scan of the AFM demonstrates nicely the accuracy of the etching process. The local change of the work function upon formation of graphene at the sidewalls has been monitored using electrostatic force microscopy (EFM) as shown in Fig. S10e. After deconvolution of the AFM tip radius the full widths of the EFM-peaks located at the facet sites represent almost the width of the GNRs.

2. Characterization by 4-tip STM SEM

The GNRs have been characterized in-situ by means of electrical transport measurements using a 4-tip STM/SEM system (Nanoprobe system, Fa. Omicron). The system operates at a base pressure of 10^{-8} Pa and by cooling with Liq-He, temperatures down to 30 K can be obtained. By means of the in-situ high-resolution SEM (<4 nm) the tungsten-tips can be navigated to desired positions above the nanostructures and approached individually to the surface via feedback control approach mechanisms. The transport measurements in this study were performed usually in the following way:

Prior to measurements on the GNRs, the W-tips (NaOH-etched) have been “calibrated” after installation. By means of sheet conductance in 2d-graphene on SiC we have ensured that the tips are mechanically stable with a geometrically small (20-40 nm radius) and metallic apex structures. As mentioned above with the help of SEM the tips have been navigated to individual ribbons and placed *above* the ribbon in a collinear arrangement with well-defined equal inter-probe spacings d . Each tip has been approached via a feedback controlled loop into a tunneling contact at its desired position (set point +2 V, 1 nA). At first hereafter, the feedback was switched off and the tips approached via calibrated piezo-elements pressing *on top* of the ribbons for the final transport measurements. After each measurement the ribbons have been carefully checked by SEM in order to exclude tip-induced changes to GNRs (and to tips).

The ex-situ processed GNR-samples have been annealed (600 °C) in-situ in order to remove organic contaminations adsorbed during transfer. Furthermore, high temperature annealing (>1300 °C) is possible in this system as well and has been used occasionally to improve further the quality, i.e. the mean free paths (the $\lambda_{\theta+}$ - see main text – Fig. 3), of the ribbons.

The selective growth of graphene nanoribbons (GNR) is demonstrated here by lateral four-probe measurements and local tunneling spectroscopy (STS). A typical tip assembly is shown in Fig. S11a). The resistances were calculated from $I(V)$ curves in a current range of $+/- 1$ μ A (cf. Fig. S11b). Most noticeably, the resistance measured on the sidewall is around 26 k Ω and almost by a factor of 20 lower compared to collinear transport measurements on the terraces (dashed line in Fig. S10a) or valleys of the MESAs. The resistances on these areas are finite, possibly due to the SiC doping, but can be well discriminated from the resistances measured at the side walls.

Local spectroscopy (STS), performed with the tip moved by the high resolution scanner in the system, has been used in addition to determine the chemical potential of the GNRs. As seen in Fig. S11c the GNR is slightly p-doped ($E_F = 150$ meV below E_D) in agreement with ARPES measurements on GNR array structures processed in a similar manner¹⁷. The fact that the chemical potential coincides de-facto with the Dirac point (ED) ensures, that only low lying subbands are occupied with electrons (see discussion below).

The STS spectrum taken on the terrace structure shows in contrast a gap of more than 1 eV at E_F . This supports our conclusions that spatially extended graphene nanostructures are formed exclusively at the step edges of the MESA structures. The onset of the current seen in the STS spectrum in the negative bias regime, which probes the occupied surface states, correlates nicely with ARPES data taken solely on buffer layer structures²¹. Please note, the STS spectra were taken by positing the tips with radii of 20-40 nm roughly above center of the GNR, thus the spectrum represents basically an average of the electronic states across the ribbon structure.

3. Additional 4-probe in-situ resistance measurement of GNR

The transport properties for various GNR structures have been systematically investigated in-situ with respect to the number of contact probes, contact separation and sample temperature. As outlined in the main text, the 0- channel start to localize for distances ≥ 150 nm. Consequently, to probe both channels requires extremely small contact spacing (< 100 nm), which is experimentally very demanding. In contrast the 0+ channel that shows a e^2/h behavior over long distance is easily measured using larger spacing.

The robustness of the ballistic behavior over long distance of the 0+ channel has been verified for many different ribbons. In total 50 different GNRs have been probed for three contact spacing in the intermediate length regime ($L = 500$ nm, 1.5 μm , and 5 μm) and various temperatures (32 K, 78 K, 120 K, 298 K). All ribbons were located within an area of $100 \times 100 \mu\text{m}^2$. Their values (absolute and relative to $G_0 = e^2/h$) are listed in Table 1 below and visualized by the histogram in Fig. S12. Most ribbons show a e^2/h conductance and the variance can be correlated with the probe spacing: Higher (lower) conductance values correspond to shorter (larger) probe spacing due to contributions of the 0. The variation within each spacing regime is attributed to slightly different mean free path for different ribbons.

Table 1 : Conductance measured on different GNRs. The absolute values, the actual probe spacing L as well as the temperature are given.

Number	Conductance (μS)	Conductance (G_0)	Probe spacing (μm)	Temperature (K)
1	58.479	1.509	0.50	298
2	36.101	0.931	5.00	298
3	34.965	0.902	5.00	298
4	49.751	1.284	1.50	298
5	41.152	1.062	5.00	298
6	45.871	1.184	1.50	298
7	29.673	0.766	5.00	298
8	34.722	0.896	5.00	298
9	36.900	0.953	0.50	298
10	40.012	1.032	1.50	298
11	48.309	1.247	5.00	298
12	50.021	1.291	1.50	298
13	37.878	0.978	5.00	298
14	38.610	0.997	5.00	298
15	43.290	1.117	1.50	298
16	44.444	1.147	5.00	298
17	44.843	1.158	0.50	298
18	48.780	1.259	5.00	298
19	55.865	1.442	0.50	298
20	62.111	1.603	0.50	298
21	37.593	0.970	1.50	120
22	35.460	0.915	5.00	120
23	37.453	0.967	5.00	120
24	41.667	1.076	1.50	120
25	43.290	1.117	5.00	120
26	42.735	1.103	1.50	120
27	46.082	1.190	1.50	120
28	56.179	1.450	0.50	120
29	59.171	1.527	0.50	120
30	54.644	1.411	1.50	120
31	39.920	1.030	5.00	120
32	39.904	1.030	1.50	120
33	38.910	1.004	5.00	120
34	45.248	1.168	0.50	120
35	40.322	1.041	1.50	120
36	40.512	1.046	1.50	32
37	35.971	0.929	5.00	32
38	31.152	0.804	5.00	32

39	35.842	0.925	5.00	32
40	37.735	0.974	5.00	32
41	37.879	0.978	1.50	32
42	40.160	1.037	5.00	32
43	38.167	0.985	5.00	32
44	44.052	1.137	0.50	28
45	43.459	1.122	0.50	28
46	35.842	0.925	5.00	298
47	40.485	1.045	5.00	298
48	39.797	1.027	1.50	78
49	39.370	1.016	1.50	78
50	37.693	0.973	0.50	78

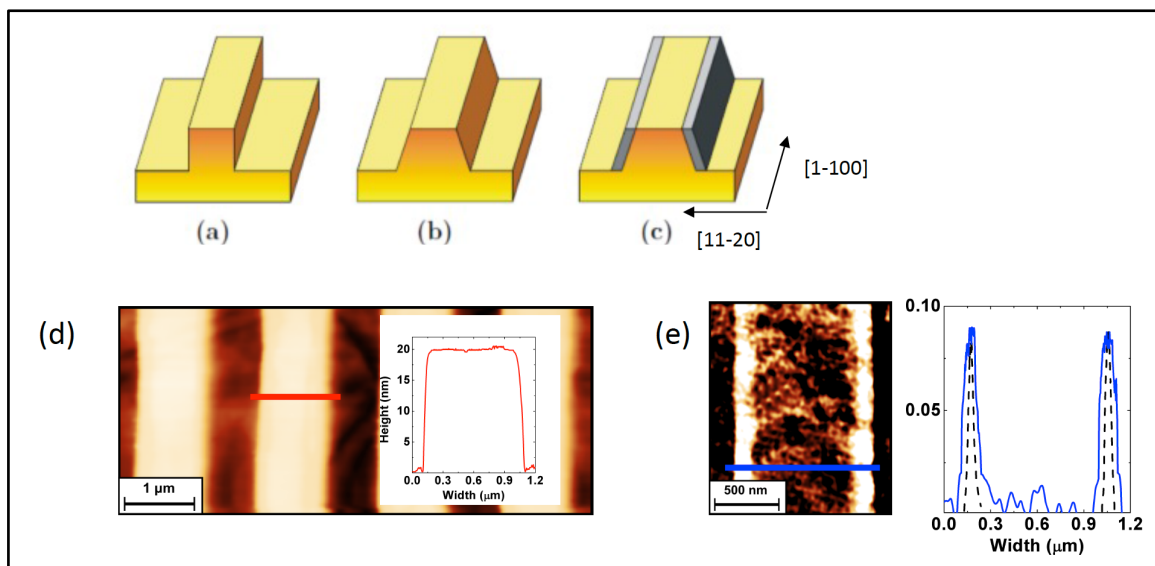


Figure S10. (a)-(c) Schematics of the MESA before (a) and after facet formation at 1420 K (b) and GNR formation at 1570 K(c). (d) AFM image of a MESA before annealing. The line scan demonstrates the successful fabrication of steep trench structures with well-defined etching depths of 20 nm. (e) EFM image taken after the final temperature step showing preferential growth of GNR at the step edges of the mesa. The dashed curve is obtained after de-convoluting of the AFM-tip shape.

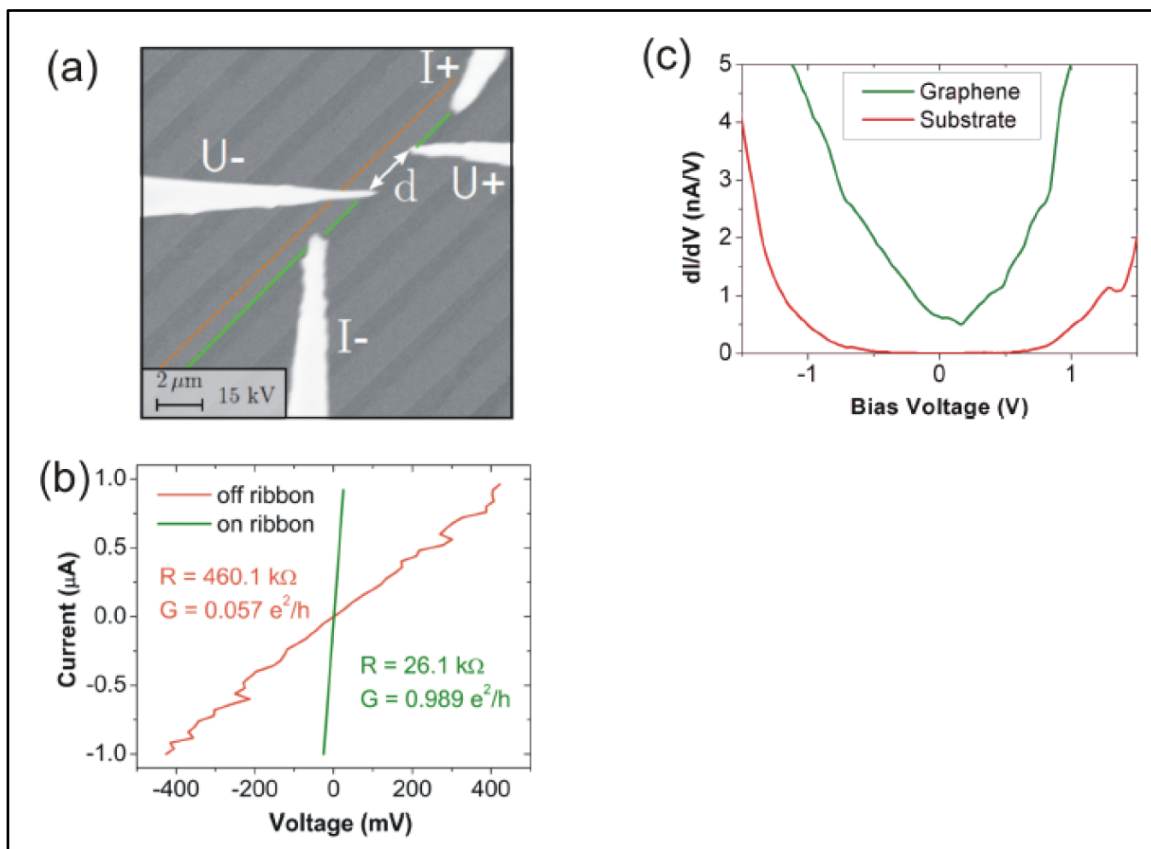


Figure S11. Demonstration of the collinear 4-probe in-situ resistance measurements. (a) SEM image of the tip positioning on top of a GNR. A current (typically $\pm 1 \mu\text{A}$) was passed to the nanostructure by using the outermost tips, while the voltage drop was measured with the inner two probes. The selective growth of GNR at the step edges is demonstrated with (b) 4-tip transport ($1 \mu\text{m}$ tip distance), showing that the resistance on the terrace is 20 times higher than on the ribbon and (c) STS (set point 1nA , 2V , measured with lock-in technique). All measurements were done at room temperature. The color codes in the different graphs correspond to each other.

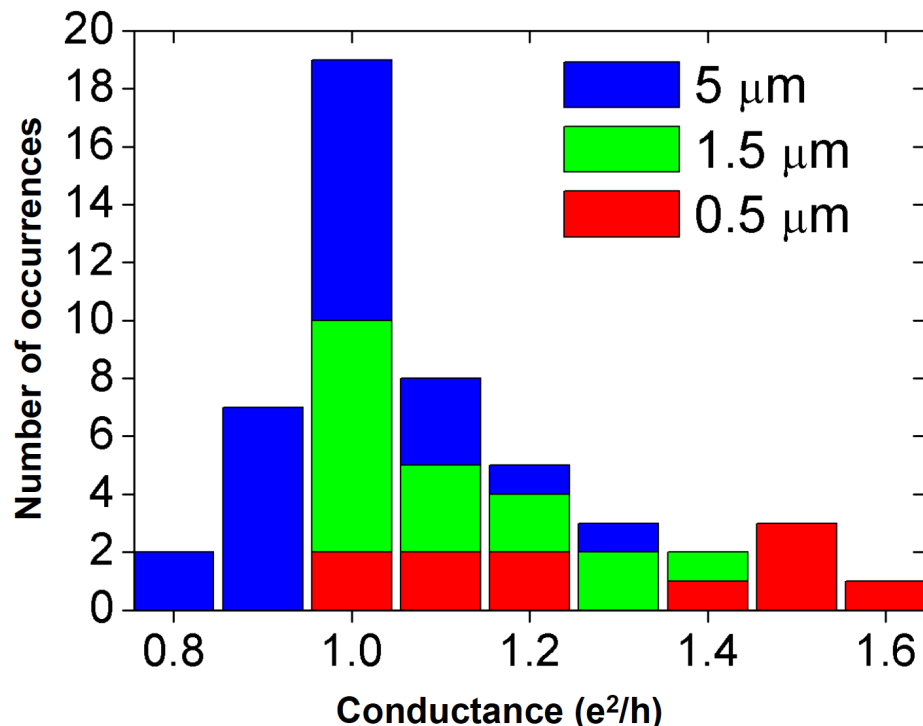


Figure S12. Histogram of the conductance values taken on 50 different GNRs and probe spacing ($L = 0.5 \mu\text{m}, 1.5 \mu\text{m}, 5 \mu\text{m}$) revealing clearly a peak at the conductance quantum e^2/h . There is a clear trend, that the smaller (larger) conductance values correspond to larger (smaller) probe spacing. The variation with temperature is extremely small (see table) and not shown here.

References for supplementary information

1. E. Stolyarova, K. T. Rim, S. M. Ryu, J. Maultzsch, P. Kim, L. E. Brus, T. F. Heinz, M. S. Hybertsen, G. W. Flynn, High-resolution scanning tunneling microscopy imaging of mesoscopic graphene sheets on an insulating surface, *P Natl Acad Sci USA* 104, 9209-9212 (2007).
2. D. L. Miller, K. D. Kubista, G. M. Rutter, M. Ruan, W. A. de Heer, P. N. First, J. A. Stroscio, Observing the Quantization of Zero Mass Carriers in Graphene, *Science* 324, 924-927 (2009).
3. K. R. Knox, S. C. Wang, A. Morgante, D. Cvetko, A. Locatelli, T. O. Mentes, M. A. Nino, P. Kim, R. M. Osgood, Spectromicroscopy of single and multilayer graphene supported by a weakly interacting substrate, *ArXiv: 0806.0355. Phys Rev B* 78, 201408(R) (2008).
4. K. R. Knox, A. Locatelli, M. B. Yilmaz, D. Cvetko, T. O. Mentes, M. A. Nino, P. Kim, A. Morgante, R. M. Osgood, Making angle-resolved photoemission measurements on

- corrugated monolayer crystals: Suspended exfoliated single-crystal graphene, *Phys Rev B* 84, 115401 (2011).
- 5. Y. M. Lin, V. Perebeinos, Z. H. Chen, P. Avouris, Electrical observation of subband formation in graphene nanoribbons, *Phys Rev B* 78, 161409(R) (2008).
 - 6. M. Y. Han, J. C. Brant, P. Kim, Electron Transport in Disordered Graphene Nanoribbons, *Phys Rev Lett* 104, 056801 (2010).
 - 7. X. R. Wang, Y. J. Ouyang, L. Y. Jiao, H. L. Wang, L. M. Xie, J. Wu, J. Guo, H. J. Dai, Graphene nanoribbons with smooth edges behave as quantum wires, *Nature Nanotechnol* 6, 563-567 (2011).
 - 8. K. Todd, H. T. Chou, S. Amasha, D. Goldhaber-Gordon, Quantum Dot Behavior in Graphene Nanoconstrictions, *Nano Letters* 9, 416-421 (2009).
 - 9. S. Frank, P. Poncharal, Z. L. Wang, W. A. de Heer, Carbon nanotube quantum resistors, *Science* 280, 1744 (1998).
 - 10. C. Schonenberger, A. Bachtold, C. Strunk, J. P. Salvetat, L. Forro, Interference and Interaction in multi-wall carbon nanotubes, *Appl Phys a-Mater* 69, 283-295 (1999).
 - 11. M. Buttiker, Four terminal phase coherent conductance, *Phys Rev Lett* 57, 1761 (1986).
 - 12. R. de Picciotto, H. L. Stormer, L. N. Pfeiffer, K. W. Baldwin, K. W. West, Four-terminal resistance of a ballistic quantum wire, *Nature* 411, 51-54 (2001).
 - 13. M. Sprinkle, M. Ruan, Y. Hu, J. Hankinson, M. Rubio-Roy, B. Zhang, X. Wu, C. Berger, W. A. de Heer, Scalable templated growth of graphene nanoribbons on SiC, *Nature Nanotechnol* 5, 727-731 (2010).
 - 14. Y. Hu, M. Ruan, Z. L. Guo, R. Dong, J. Palmer, J. Hankinson, C. Berger, W. A. de Heer, Structured epitaxial graphene: growth and properties, *J. Phys D* 45, 154010 (2012).
 - 15. M. Ruan, Y. Hu, Z. Guo, R. Dong, J. Palmer, J. Hankinson, C. Berger, W. A. de Heer, Epitaxial graphene on silicon carbide: Introduction to structured graphene, *MRS Bulletin* 37, 1138 (2012).
 - 16. M. Ruan, "Structured epitaxial graphene for electronics," School of Physics, PhD dissertation- Georgia Institute of Technology -<http://hdl.handle.net/1853/45596>, Atlanta, July 2012.
 - 17. J. Hicks, A. Tejeda, A. Taleb-Ibrahimi, M. S. Nevius, F. Wang, K. Shepperd, J. Palmer, F. Bertran, P. Le Fèvre, J. Kunc, W. A. de Heer, C. Berger, E. H. Conrad, A wide-bandgap metal–semiconductor–metal nanostructure made entirely from graphene, *Nature Phys* 9, 49-54 (2013).
 - 18. C. W. J. Beenakker, H. Vanhouten, Quantum Transport in Semiconductor Nanostructures, *Solid State Phys* 44, 1-228 (1991).
 - 19. W. Norimatsu, M. Kusunoki, Formation process of graphene on SiC (0001), *Physica E* 42, 691-694 (2010).
 - 20. W. A. de Heer, C. Berger, M. Ruan, M. Sprinkle, X. Li, Y. Hu, B. Zhang, J. Hankinson, E. H. Conrad, Large area and structured epitaxial graphene produced by confinement controlled sublimation of silicon carbide, 108, 16900-16905 (2011).
 - 21. K. V. Emtsev, T. Seyller, F. Speck, L. Ley, P. Stojanov, J. D. Riley, R. G. C. Leckey, Initial stages of the graphite-SiC(0001) interface formation studied by photoelectron spectroscopy *Mat Sci Forum* 55, 6525 (2006).